LUPINE PUBLISHERS

Modern Approaches on Material Science

DOI: 10.32474/MAMS.2020.03.000155

ISSN: 2641-6921

Short Communication

Monitoring Time-Progression of Structural, Magnetic Properties of Ni Nano Ferrite During Synthesis

Verma R and Kane SN*

Magnetic materials laboratory, School of Physics, D. A. University, Khandwa Road, Indore, 452001, India

***Corresponding author:** Kane SN, Magnetic materials laboratory, School of Physics, D.A. University, Khandwa Road, Indore, 452001, India

Received: June 09, 2020 **Published:** July 07, 2020

Abstract

We present time-progression of structural, magnetic properties of $NiFe_2O_4$ nano ferrite during its synthesis via sol-gel auto combustion technique, monitored by x-ray diffraction XRD, and magnetic measurements. XRD patterns of the samples collected between 18-52 minutes shows the formation of the nano spinel phase (grain diameter: 15.4 nm-28.6 nm), presence of α –Fe_2O_3 phase was also detected. Samples collected between 8-14 minutes show the amorphous nature of the samples. Time-progression studies show: a) sample taken after 20 minutes shows a sharp decrease of specific surface area (range between 39.01 m2/g to 72.73 m^2/g), b) non-equilibrium cationic distribution for samples taken between 16-20 minutes with a continuous increase of Fe^{3+} ions population on B-site with simultaneous decrease of Ni^{2+} population, c) for samples taken after 22, 52 minutes, cationic distribution is close to its ideal value of (Fe^{3+}) $[Ni^{2+}Fe^{3+}]$, d) alteration of a degree of inversion (δ), oxygen parameter (u), modification of A-O-B, A-O-A, B-O-B super-exchange interactions, e) ferrimagnetically aligned core, and spin disorder on the surface with a thickness between 1.9 nm to 3.6 nm, reducing the saturation magnetization (ranging between 11.7 - 25.5 Am^2/kg), as compared to bulk Ni ferrite (55 Am^2/kg), f) low squareness ratio values (0.15-0.22) shows the presence of multi-domain nanoparticles, with coercivity between 111-157 Oe.

Keyword: Time-evolution of properties; Sol-gel auto combustion synthesis; XRD; Nano Ni ferrite; Cationic distribution; Magnetic properties

Introduction

Spinel ferrites with general formula $Me^{2+}O.Fe^{3+}{}_2\ O_3$, [Me: Divalent metal ion e.g. – Ni^{2+}, Zn^{2+}, Mg^{2+} Co^{2+} etc.], display face-centered cubic (fcc) structure, with two inter-penetrating sub-lattices: tetrahedrally coordinated (A site), octahedrally coordinated (B site) [1]. Nickel ferrite ($NiFe_2O_4$) has inverse spinel structure expressed as: (Fe^{3+}) $[Ni^{2+}Fe^{3+}]$ [1]. Allocation of cations on A, B site is crucial in determining properties of spinel ferrites [2,3], can be effectively used to achieve desired properties. Literature gives Ni ferrite synthesis using various methods including mechanical milling [4], coprecipitation [5], hydrothermal synthesis [6], sol-gel auto combustion method [7], showing the effect of the technique on structural, magnetic properties. Literature also reports real-time monitoring (in-situ studies) of properties [8,9], require special, sophisticated equipment, may not be available in all laboratories. Ex-situ monitoring of properties [10], describing the time-evolution of structural, magnetic properties, is a rather simple, more convenient way to perform experiments by utilizing standard laboratory equipment available in many laboratories. Ni ferrite is used in magnetic resonance imaging (MRI) agents [5], photocatalysis for water purification, antimicrobial activity [11], etc.) hence tuning its properties are preferred for improved efficiency. So, in this work, we present the time-development of structural, magnetic properties of $NiFe_2O_4$ nano ferrite during its synthesis via sol-gel auto combustion technique. Prepared samples are investigated via x-ray diffraction 'XRD,' vibration sample magnetometry, to get complimentary information on structural, magnetic properties.

Experimental Details

$NiFe_2O_4$ ferrite samples were synthesized by the sol-gel auto-combustion protocol, as described in detail in [12], by utilizing

AR grade -nitrate/acetate-citrate precursors: Nickel acetate - $Ni(CH_3CO_2)_2{\cdot}4H_2O$, Ferric nitrate ($Fe(NO_3)_3.9H_2O$), Citric acid - $C_6H_8O_7$]. The precursors were mixed in the stoichiometric ratio, were dissolved in 10 ml de-ionized water by keeping metal salts to fuel (citric acid) ratio as 1:1. At the same time, the solution pH was maintained at 7. Now the solution was heated at ~110°C. As dry gel starts to form (taken as 0 minutes) small part of the sample is taken out from the reaction vessel (in an interval of 8, 10, 12, 14, 16, 18, 22, and 52 minutes), and were immediately ice-quenched to room temperature. Powder samples were used for Cu-K- X-ray diffraction 'XRD' measurements (Bruker D8 diffractometer), hysteresis loops by vibrating sample magnetometer. Full-profile XRD analysis was done by MAUD Rietveld refinement software [13] to obtain the lattice parameter (apex.). XRD analysis gives Scherrer's crystalline size D (calculated by the integral width of 311 peak, corrected for instrumental broadening), specific surface area (S), inversion parameter (δ), oxygen parameter (u). XRD data was also analysed to get cationic distribution via Bertaut method [14], This provides cationic distribution by comparing experimental and computed intensity ratio of planes I(220)/I(400) and I(400)/I(422), susceptible to cationic distribution [12]. Cationic distribution was used to calculate theoretical or Néel magnetic moment at 0K (Ms(th)), theoretical lattice parameter (ath.), bond angles (θ_1, θ_2, θ_3, θ_4, θ_5) as shown in [3]. Coercivity (Hc), saturation magnetization (Ms), remanence (Mr), squareness ratio (Mr/Ms) was obtained from hysteresis loops. (Figure 1) gives the schematic of sample synthesis and characterization.

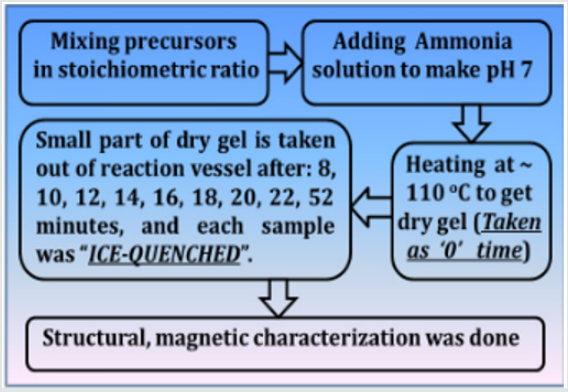

Figure 1: Schematic of sample synthesis and characterization.

Results and Discussion

(Figure 2) (a) gives XRD-patterns of the studied $NiFe_2O_4$ samples collected after 18, 20, 22, and 52 minutes, confirm the formation of the spinel phase. XRD patterns also show the presence of α-Fe_2O_3 phase, ascribable to sample synthesis at a reasonably lower temperature (~110 °C), as reported in [15], while its disappearance is seen after higher sintering temperature. Figure 1(a) inset shows XRD patterns of samples collected after 8, 10, 12, 14 minutes show the amorphous nature of the samples. Only in the sample collected after 14 minutes, there is the start of spinel phase formation (indicated by a dotted circle). Illustrative Rietveld refined XRD pattern (Figure 2) b) of $NiFe_2O_4$ sample taken after 20 minutes also validates the cubic spinel ferrite phase formation. (Figure 2) (c) shows a variation of D (range between 15.4 nm to 28.6 nm) and S (range between 39.01 m^2/g to 72.73 m^2/g) for $NiFe_2O_4$ samples taken after 16, 18, 20 22, 52 minutes. A perusal of (Figure 2) (c) shows a well-known inverse relationship shown by the expression: [$S = [6/(D \times \rho_{XRD})]$], where ρ_{XRD} is x-ray density, as was also reported in [2]. (Figure 2) (c) shows that for samples taken after 22, 52 minutes, D sharply increases with concurrent reduction of S, is ascribable to significant changes in cationic distribution via migration of Ni^{2+} ions to B site with simultaneous migration of Fe^{3+} ions on A site(as can be seen in Table 1). (Figure 2)(c) inset display linear relation between δ and u as was also observed earlier [3], shows that reduction of the degree of inversion (δ) leads to a reduction of oxygen parameter (u), a measure of disorder in the studied system, is expected to affect the properties of the studied samples. Table 1 depicts the variation of experimental and theoretical lattice parameter ($a_{exp.}$, $a_{th.}$), inversion parameter (δ), oxygen parameter (u), Cation distribution (for A, B site), and calculated, observed intensity ratios for I400/422, I220/400 plane for the studied samples. The observed variation of $a_{exp.}$ is consistent with changes in cationic distribution, and variation of the degree of inversion (δ). Close agreement between observed, calculated $a_{exp.}$, $a_{th.}$ suggests that the computed cationic distribution agrees well with real distribution [16]. Close matching of calculated, observed intensity ratios for I400/422, I220/400 signifies an accurate cationic distribution among A, B site [17]. Cationic distribution illustrates that as we go from $NiFe_2O_4$ samples taken after 16, 18, and 20 minutes, the population of Fe^{3+} ions on B site increases from 1.2 to 1.5 with a concurrent decrease of Ni^{2+} ions from 0.80 to 0.50. For samples taken after 22, 52 minutes Fe^{3+} population on B site decreases, while Ni^{2+} ion population increases up to 0.98, which is close to the ideal inverse cationic distribution of (Fe^{3+}) [$Ni^{2+}Fe^{3+}$] [1].

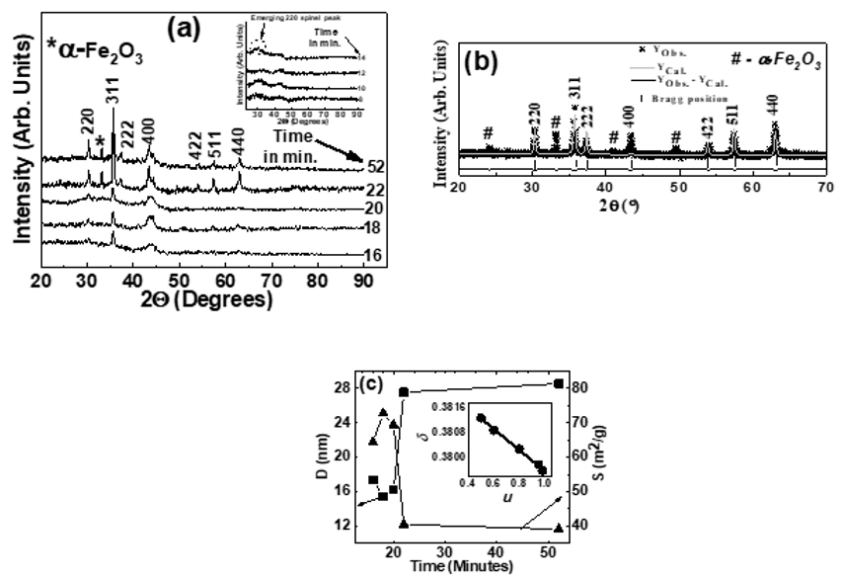

Figure 2: (a): XRD patterns of the studied $NiFe_2O_4$ samples taken after 16, 18, 20 22, 52 minutes showing the formation of the spinel phase. Inset: XRD patterns of the studied samples taken after 8, 10, 12, 14 minutes. (b): Illustrative Rietveld refined XRD pattern of $NiFe_2O_4$ sample taken after 20 minutes (* – *Experimental data, Solid line – theoretically analyzed data,* | – *Bragg peak positions, Bottom line – Difference between experimental, and fitted data*). (c) variation of grain diameter (D) and specific surface area (S) for $NiFe_2O_4$ samples taken after 16, 18, 20 22, 52 minutes. Line connecting points guide to the eye. Inset: variation of inversion parameter (δ) with oxygen parameter (u). The straight line is a linear fit to the experimental data.

Figure 3 depicts the variation of bond angles between cations, cation-anion θ_1, θ_2, θ_3, θ_4 and θ_5, for the studied samples taken between 16 - 52 minutes. In samples taken after 8, 10, 12, and 14 minutes, due to the absence of the spinel phase, bond angles could not be computed. Bond angles provide information on super-exchange interaction (A-O-B, A-O-A, B-O-B), mediate by oxygen. (Figure 3) shows that for samples taken after 16, 16, 20 minutes θ_1, θ_2, θ_5, decreases while θ_3, θ_4 increases, indicates a weakening of A–O–B, A– O–A and strengthening B–O–B super-exchange interaction as is also observed earlier [16]. For samples taken after 22, 52 minutes θ_1, θ_2, θ_5, increases, and θ_3, θ_4 decreases reveals strengthening of A-O-B, A-O-A, and weakening of B-O-B super-exchange interaction, reported in the literature with compositional changes [3]. Samples taken after different times, there is a modification of A-O-B, A-O-A, B-O-B super-exchange interactions, are attributed to changes in δ and u as shown in (Table 1), observed with compositional changes [3,16]. Observed A-O-B, A-O-A, B-O-B super-exchange interactions should mirror in magnetic properties, matches well with reported literature [3,16]. Thus, collecting samples after different times during synthesis is analogous to compositional changes in spinel ferrites, affects structural, magnetic properties [3, 12, 16, 18].

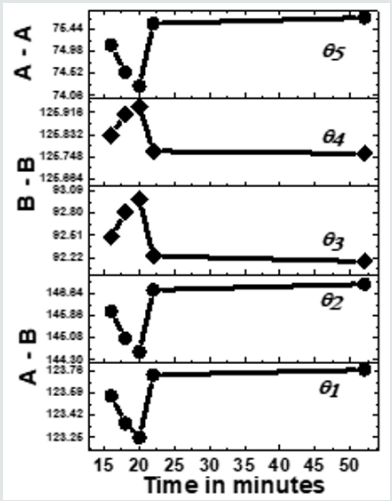

Figure 3: Dependence of bond angles ($\theta_1^{A\text{-}O\text{-}B}$, $\theta_2^{A\text{-}O\text{-}B}$, $\theta_3^{B\text{-}O\text{-}B}$, $\theta_4^{B\text{-}O\text{-}B}$, $\theta_5^{A\text{-}O\text{-}A}$) for $NiFe_2O_4$ samples taken after 16, 18, 20 22, 52 minutes. Line connecting points guide to the eye.

Figure 4 depicts hysteresis loops, reveal changes in $Ms_{(exp.)}$ samples taken after 16, 18, 20 22, 52 minutes, attributable to alteration of B-O-B, A-O-B, and A-O-A interaction, depends on bond angles, as shown in (Figure 3), and cationic distribution, as shown in (Table 1). (Figure 4) inset displays hysteresis loops of the samples taken after 8, 10, 12, 14 minutes, showing very low magnetization, attributable to the fact that in these samples ferrite phase is not formed, as was also observed in XRD data shown inset of (Figure 2) (a). Observed lower values of $M_{s(exp.)}$ (*ranging between 11.7 - 25.5 Am^2/kg*) as compared to the multi-domain bulk Ni ferrite (55 Am^2/kg) is attributed to the two-component nanoparticle system as described in [19] consisting of a spin-disorder on the surface layer and ferrimagnetically aligned spins within the core. Computed magnetic dead layer thickness as described in [20,21] for $NiFe_2O_4$ samples taken after 16, 18, 20 22, 52 minutes are respectively 2.3, 1.8, 1.9, 2.5 and 3.6 nm. They confirm the contribution of '*dead layer thickness*' in the reduction of $M_{s(exp.)}$, apart from B-O-B, A-O-B, and A-O-A super-exchange interaction and cationic distribution.

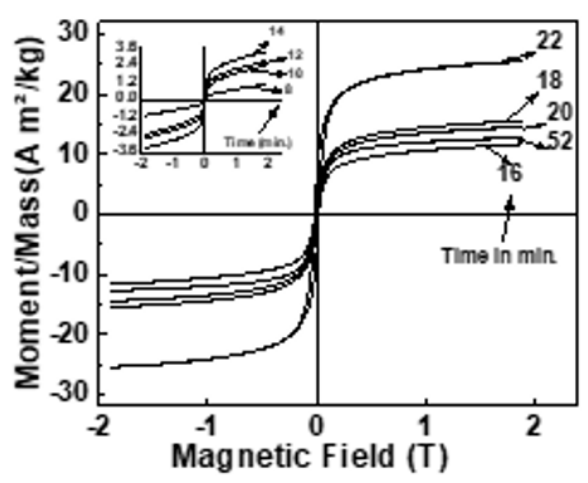

Figure 4: Hysteresis loops of the studied $NiFe_2O_4$ samples taken after 16, 18, 20 22, 52 minutes. Inset: Hysteresis loops of the samples taken after 8, 10, 12, 14 minutes.

Table 1: Variation of experimental and theoretical lattice parameter ($a_{exp.}$, $a_{th.}$), inversion parameter (δ), oxygen parameter (u), Cation distribution (for A, B site), and observed, calculated intensity ratios for I400/422, I220/400 plane for the studied samples.

Time	aexp	ath	δ	u	Cation distributions	$I_{220/400}$		$I_{400/422}$	
(Minutes)	(nm)	(nm)				Cal.	Obs.	Cal.	Obs.
16	0.8341	0.8345	0.8	0.3803	$(Ni^{2+}_{0.20}Fe^{3+}_{0.80})A$ $[Ni^{2+}_{0.80}Fe^{3+}_{1.20}]B$	0.8	0.79	1.22	1.35
18	0.8352	0.8352	0.6	0.3809	$(Ni^{2+}_{0.40}Fe^{3+}_{0.60})A$ $[Ni^{2+}_{0.60}Fe^{3+}_{1.40}]B$	0.88	0.75	1.31	1.4
20	0.8334	0.8355	0.95	0.3798	$(Ni^{2+}_{0.50}Fe^{3+}_{0.50})A$ $[Ni^{2+}_{0.50}Fe^{3+}_{1.50}]B$	0.95	0.89	1.25	1.31
22	0.8357	0.834	0.5	0.3813	$(Ni^{2+}_{0.05}Fe^{3+}_{0.95})A$ $[Ni^{2+}_{0.95}Fe^{3+}_{1.05}]B$	0.76	0.81	1.24	1.31
52	0.8335	0.8339	0.98	0.3796	$(Ni^{2+}_{0.02}Fe^{3+}_{0.98})A$ $[Ni^{2+}_{0.98}Fe^{3+}_{1.02}]B$	0.84	0.74	1.41	1.52

Figure 5 (a) depicts Variation of $M_{s(exp.)}$, $M_{s(th.)}$ for $NiFe_2O_4$ samples taken after 16, 18, 20 22, 52 minutes. A perusal of figure 5(a) shows that observed behaviour is attributable to alteration of B-O-B, A-O-B, and A-O-A super-exchange interaction, depends on bond angles (see figure 3), and cationic distribution (see Table 1). Non-similar trend of $M_{s(exp.)}$, $M_{s(th.)}$ in (Figure 5) (a), shows that the magnetization behaviour is governed by Yafet-Kittel three sub-lattice model, described in [22], confirmed by the computed canting angle ($\alpha_{Y\text{-}K}$) values for $NiFe_2O_4$ samples taken after 16, 18, 20 22, 52 minutes, which are respectively 52.7, 56.6, 46.2, 55.7, 46.9°. The canting angle provides information on spin canting on the surface, is so-called '*magnetic dead layer*,' leads to a reduction of $M_{s(exp.)}$, which is lower than bulk saturation magnetization of Ni ferrite (55 Am^2/kg). Inset of Figure 5 (a) shows the variation of $M_{s(exp.)}$ with oxygen parameter '*u*'(*which is a measure of disorder in the samples* [1]). Figure 5 (a) shows the disorder-induced enhancement of $M_{s(exp.)}$, as was also reported in [3]. (Figure 5) (b) depicts the Coercivity (H_c) variation for $NiFe_2O_4$ samples taken after 16, 18, 20 22, 52 minutes.

Obtained H_c and related *D* values imply that studied samples lie in the region with overlap between single or multi-domain structures, as reported earlier [3]. (Figure 5) (b) Inset depicts the variation of Mr/Ms for $NiFe_2O_4$ samples taken after 16, 18, 20 22, 52 minutes. Mr/Ms values ranging between 0.15-0.22 reveal enhanced inter-grain interactions suggesting isotropic behavior of the material [23] reveal multi-domain particles with no preferential magnetization direction. Time-dependent tunable structural, magnetic properties during synthesis are valuable in achieving optimal properties of Ni ferrite for their usage in magnetic resonance imaging [5], hyperthermia [24] for cancer treatment, photocatalysis for water purification [11].

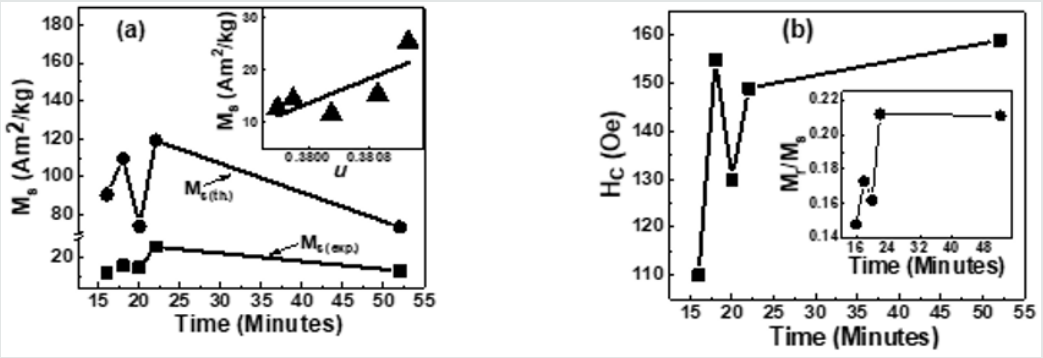

Figure 5: (a) Variation of $Ms_{(exp.)}$, $Ms_{(th.)}$ for $NiFe_2O_4$ samples taken after 16, 18, 20 22, 52 minutes. Inset: Dependence of $Ms_{(exp.)}$ on oxygen parameter (u), line connecting points in Inset are linear fit to the experimental data.; (b) Coercivity (H_c) variation for $NiFe_2O_4$ samples taken after 16, 18, 20 22, 52 minutes. Inset: Variation of *Mr/Ms* for $NiFe_2O_4$ samples taken after 16, 18, 20 22, 52 minutes.

Summary

To summarize, the sol-gel auto combustion technique is used to observe the time-development of structural, magnetic properties of Ni ferrite. Changes in cationic distribution lead to modification of structural properties, magnetic interactions, responsible for observed magnetic properties. Time-progression of properties are of use to alter structural, magnetic properties of Ni ferrite as a material for its prospective usage in heterogeneous catalysis, water purifications, biomedical applications.

Acknowledgments

Authors thank Dr. M. Gupta-L. Behra, UGC-DAE CSR, Indore for XRD measurements. Work supported by UGC-DAE CSR, Indore project (No.: CSR-IC-ISUM-25/CRS-308/2019-20/1360, dated March 5, 2020).

Conflicts of Interest

The authors declare no conflict of interest.

Author Contributions

Conception: SNK; Sample synthesis, RV, SNK; Measurements, analysis of data: SNK, RV; Supervision, Resources, supervision, project management: SNK; Writing the manuscript: SNK, RV. All authors approve the draft and participate in reviewing.

References

1. Smit J, Wijn HPJ (1959) Ferrites, Philips Technical Library, Eindhoven, Holland, P.137.
2. Raghuvanshi S, Mazaleyrat F, Kane SN (2018) Mg1-xZnxFe$_2$O$_4$ nanoparticles: Interplay between cation distribution and magnetic properties. AIP Adv 8(4).
3. Kane SN , Satalkar M (2017) Correlation between magnetic properties and cationic distribution of Zn0.85-x NixMg0.05Cu0.1Fe$_2$O$_4$ nano spinel ferrite: effect of Ni doping. J Mater Sci 52: 3467-3477.
4. Shi Y, Ding J, Liu X, Wang J (1999) $NiFe_2O_4$ ultrafine particles prepared by coprecipitation/mechanical alloying. J Magn Magn Mater 205: 249-254.
5. Ahmad T, Rhee I, Hong S, Chang Y, Lee J (2011) Ni-Fe_2O_4 Nanoparticles as Contrast Agents for Magnetic Resonance Imaging. J Nanosci and Nanotech. 11: 5645-5650.
6. Zhou J, Ma J, Sun C, Xie L, Zhao Z, et al. (2005) Low-Temperature Synthesis of $NiFe_2O_4$ by a Hydrothermal Method. J Am Ceram Soc 88: 3535-3537.
7. Kane SN, Raghuvanshi S, Satalkar M, Reddy VR, Deshpande e UP t al. (2018) Synthesis, characterization, and antistructure modelling of Ni nano ferrite. AIP Conf Proc 1953(1).
8. Strom V, Olsson RT, Rao KV (2010) Real-time monitoring of the evolution of magnetism during precipitation of superparamagnetic nanoparticles for bioscience applications. J Mater Chem 20: 4168- 4175.
9. Fernández-Garcia MP, Teixeira JM, Machado P, Oliveira MRFF, Maia JM, et al. (2015) Automatized and desktop AC-susceptometer for the in situ and real-time monitoring of magnetic nanoparticles' synthesis by coprecipitation. Rev Sci Instrum 86(4).
10. Raghuvanshi S, Mazaleyrat F, Kane SN (2017) Time Evolution of Structural and Magnetic Properties of Ni-Zn Nano Ferrite: An Opinion. JOJ Material Sci 1(2).
11. Naik MM, Naik HSB, Kottam N, Vinuth M, Nagaraju G et al. (2019) Multifunctional properties of microwave-assisted bioengineered nickel doped cobalt ferrite nanoparticles. J Sol-Gel Sci Tech 91: 578-595.
12. Tiwari P, Verma R, Kane SN, Tatarchuk T, Mazaleyrat F (2019) Effect of Zn addition on structural, magnetic properties and anti-structural modeling of magnesium-nickel nano ferrites. Mater Chem Phys 229: 78-86.
13. Lutterotti L, Scardi P (1990) Simultaneous structure and size-strain refinement by the Rietveld method. J Appl Cryst 23: 246-252.
14. Bertaut EF (1950) Etude de la nature des ferrites spinelles. Comptes Rendus Hebdomadaires des Séances de l'Academie des Sciences 230: 213-215.

15. Kumar ER, Jayaprakash R (2013) Effect of combustion rate and annealing temperature on structural and magnetic properties of manganese substituted nickel and zinc ferrites. J Magn Magn Mater 348: 93-100.

16. Verma R, Kane SN, Tiwari P, Modak SS, Tatarchuk T et al. (2018) Ni addition induced modification of structural, magnetic properties and antistructural modeling of Zn1-xNixFe_2O_4 (x = 0.0-1.0) nanoferrites. Mol Cryst Liq Cryst 674 (1): 130-141.

17. Satalkar M, Kane SN, Kumareravenji M, Araujo JP (2017) On the role of cation distribution in determining magnetic properties of Zn0.7-xNixCu0.1Fe_2O_4 nano ferrite., Mater Res Bull 91: 14-21.

18. Maaz K, Karim S, Mashiatullah A, Liu J, Hou MD (2009) Structural analysis of nickel doped cobalt ferrite nanoparticles prepared by coprecipitation route. Physica B 404: 3947-3951.

19. Kale A, Gubbala S, Misra RDK (2004) Magnetic behavior of nanocrystalline nickel ferrite synthesized by the reverse micelle technique. J Magn Magn Mater 277: 350-358.

20. Chen JP, Sorense CM, Klabunde KJ, Hadjipanayis GC, Devlin E, et al. (1996) Size-dependent magnetic properties of $MnFe_2O_4$ fine particles synthesized by coprecipitation. Phys Rev B Condens Matter 54: 9288-9296.

21. Rabi B, Essoumhi A, Sajieddine M, Greneche JM, Hlil EK, et al. (2020) Structural, magnetic and magnetocaloric study of Ni0.5Zn0.5Fe_2O_4 spinel. Appl Phys A 126: 174.

22. Murthy NSS, Natera MG, Youssef SI, Begum RJ, Srivastava CM (1969) Yafet-Kittel angles in zinc-nickel ferrites. Phys Rev 181: 969-977.

23. Shirsath SE, Toksha B, Jadhav K (2009) Structural and magnetic properties of In^{3+} substituted $NiFe_2O_4$. Mater Chem Phys 117: 163-168.

24. Barrera G, Coisson M, Celegato, Martino FL, Tiwari P et al. (2020) Specific Loss Power of Co/Li/Zn-Mixed Ferrite Powders for Magnetic Hyperthermia. Sensors 20(7): 2151.

DOI: 10.32474/MAMS.2020.03.000155